nature chemistry

SUPPLEMENTARY INFORMATION

DOI: 10.1038/NCHEM.2886

In the format provided by the authors and unedited.

Theory-driven design of high-valence metal sites for water oxidation confirmed using *in situ* soft X-ray absorption

Xueli Zheng†, Bo Zhang†*, Phil De Luna†, Yufeng Liang, Riccardo Comin, Oleksandr Voznyy, Lili Han, F. Pelayo García de Arquer, Min Liu, Cao Thang Dinh, Tom Regier, James Dynes, Sisi He, Huolin L. Xin, Huisheng Peng, David Prendergast, Xiwen Du and Edward H. Sargent*

†These authors contributed equally to this work

*Correspondence and requests for materials should be addressed to Edward H. Sargent (ted.sargent@utoronto.ca) (E.H.S) and (boo.zhang@utoronto.ca) (B.Z.)

Contents:

Theoretical Calculations.

Energetics Calculations

The initial structure of $Ni(OH)_2$ was taken from literature reports[36], while β-NiOOH was chosen with staggered intercalating protons in light of recent work[23] that found that a stable low-spin d^7 Ni^{3+} configuration was consistent with experimental crystal structures. For NiO_2, the initial structure was derived from the crystal structure of $Ni(OH)_2$ with all protons deleted from the unit cell. Full geometry and unit cell optimizations were performed on the base $Ni(OH)_2$, β-NiOOH, and NiO_2 structures before adding the effect of metal and phosphorus doping. The Gibbs free energy of formation, $\Delta G°_f$, was calculated using the framework of Persson et al.[17] that has previously been used to study Co oxides and (Ni,Fe)OOH for OER energetics[13, 24]. Bulk energetics of metal and phosphorous doped Ni-oxides were calculated using density functional theory (DFT) with the Hubbard-*U* framework (DFT+U) to account for the strongly localized *d*-electrons for Ni, Fe, and Co[37]. The Hubbard-*U* correction terms were fixed at U_{hub}(Ni) = 6.45 eV, U_{hub}(Co) = 3.32 eV, and U_{hub}(Fe) = 5.3 eV as obtained via linear response theory[38]. These values were taken from previous studies on Ni,Fe(OOH) and Co oxides[13, 22, 24]. Furthermore, it has been shown that varying U_{hub}(Ni) values between 2.5 eV to 7 eV showed no qualitative change in optimized lattice parameters[22]. The Perdew-Burke-Ernzerhof (PBE) exchange-correlation functional[39] and Blöchl's all-electron, frozen-core, projector augmented (PAW) method[40,41] with a plane-wave basis set cutoff value of 750 eV were used with the Vienna Ab-initio Simulation Package (VASP)[42]. PAW potentials were in effect for the 4s/3d electrons of Ni, Co, Fe, and the 2s/2p electrons of O, while all other core electrons were kept frozen. The total energy was considered converged once the energy difference reached below 1 meV/atom. Γ-point-centered Monkhorst−Pack[44] was used and only the gamma point was sampled for the k-points for optimizations. Bulk structures were 6x2x2 supercells and were converged below a force threshold of 0.01 eV/Å with Gaussian smearing and a smearing width of 0.05 eV. For density of states, a 3x9x9 Γ-point-centered Monkhorst−Pack k-point mesh was used. The

computational hydrogen electrode (CHE) was used to calculate the change in free energies (ΔG) for the oxidation of $Ni^{2+} \rightarrow Ni^{3+}$ and $Ni^{3+} \rightarrow Ni^{4+}$.

Optimized $Ni(OH)_2$ lattice constants match well with experiment[39] and β-NiOOH lattice constants agreed with the previous DFT study with intercalated protons[22]. Table S1 shows lattice constants for all optimized structures. First, binary mixtures were modeled by random substitution of two Ni atoms in 6x2x2 lattice structures of $Ni(OH)_2$, β-NiOOH, and NiO_2 with Co and Fe. Ternary mixtures were made through random substitution of four Ni atoms, two for Fe and two for Co. Next, NiO_2H_x, $NiCoO_2H_x$, and $NiCoFeO_2H_x$ structures were doped with phosphorus through substitution of one Ni atom for a P in order to mimic the incorporation of a phosphate in the bulk structure. All doped structures were also allowed to be fully optimized.

Spin polarized calculations were performed on all structures. Initial $Ni(OH)_2$, NiOOH, and NiO_2 starting structures were chosen with anti-ferromagnetic arrangement which was previously shown to be preferred compared to the ferromagnetic or parallel spin configurations[22]. The magnetic moments for each nickel ion in the optimized low spin structures was found to be approximately ± 1.8 μ_B, ± 1.2 μ_B, and ± 0 μ_B for $Ni(OH)_2$, NiOOH, and NiO_2 respectively. The magnetic moment for NiOOH is similar to previously published low-spin magnetic moment of ± 1.5 μ_B from ab-initio calculations[22].

Since the experimental catalyst is mainly amorphous, we are not able to provide a structural model at long range using DFT. Thus, we have decided to use a model system, with the assumption of the preservation of local chemistry, to elucidate trends with respect to doping of other elements. γ-phase is significantly more complex to model computationally due to the larger number of possible intercalating species and different stacking orientations of the NiO_x sheets. To properly and thoroughly model all possible configurations of doped γ-NiO_x would be prohibitively time intensive. Furthermore, there has been extensive work on the structural and electronic features of β-$Ni(OH)_2$ and β-NiOOH on which we could lean to ensure accuracy of our models[42, 43]. Therefore, we believe that the use of the β-phase is justified in this study.

The balanced chemical reaction was calculated at pH=0 and was referenced against the standard hydrogen electrode. Therefore, for a given nickel oxyhydroxide the oxidation reaction is ($NiO_xH_y \rightarrow NiO_xH_{y-1} + H^+ + e^-$) and the reduction reaction is ($2(H^+ + e^-) \rightarrow H_2$). The Gibbs free energy of the H^+ is accounted for in the chemical potential of a proton as calculated in the framework provided by Persson et al[14]. Simply, we begin with oxygen and hydrogen in equilibrium with water in an aqueous environment, $½\ O_{2(g)} + H_{2(g)} \leftrightarrow H_2O_{(l)}$. Next the chemical potential of water is written as a function of the oxygen and hydrogen Gibbs free energies, $\mu_{H2O} = \Delta G_{H2O} = G_{H2O} - G_{H2} - ½\ G_{O2}$. The reference Gibbs free energy for hydrogen is now $G_H = ½\ [G_{H2O} - \Delta G_{H2O} - ½\ G_{O2}]$. The chemical potential of hydrogen in the standard state can now be written as $\mu H = ½\ [E_{H2Odft} - TS_{H2O} - \mu_O - \mu H2O_{ref}]$ where E_{H2Odft} = -14.7 eV, T = 298 K, S_{H2O} = 7.24 x 10^{-4} eV/K, μ_O = -4.57 eV, μH_2O_{ref} = -2.46 eV and μH = -3.73 eV. This value is consistent with our calculations because we have used the same DFT package (VASP) implemented with the identical PBE GGA functional and the same convergence cutoffs of 5 meV/atom.

The Gibbs energy of formation ($\Delta G°_f$) for a nickel oxyhydroxide is outlined below as $\Delta G°_f (NiO_xH_y) = E_{NiOxHy} - E_{Ni} - xE_O - yE_H$ where E_{Ni} is -7.6 eV (calculated from bulk nickel), E_O is -4.57 eV (calculated from water), and E_H is -3.73 eV (as calculated from water described above). The Gibbs energies of formation are listed in table S2.

The Gibbs energy of oxidation from Ni^{2+} to Ni^{3+} ($\Delta G_{(Ni2+ \rightarrow Ni3+)}$) is calculated as $\Delta G_{(Ni2+ \rightarrow Ni3+)} = E_{NiOOH} - E_{Ni(OH)2} - \mu H$ where E_{NiOOH} is the energy of NiOOH as calculated from DFT, $E_{Ni(OH)2}$ is the energy of $Ni(OH)_2$ as calculated from DFT, and μH is the chemical potential of hydrogen. The entropy was not calculated for the bulk catalyst since the energy contributions due to the vibrations of the bulk are very small in comparison to water or hydrogen[35].

We believe this value is consistent with our calculations because we have used the same DFT package (VASP) implemented with the PBE GGA functional and the same convergence cutoffs of 5 meV/atom. Supplementary Table 2 shows the DFT energies per formula unit and the formation free energies for all bulk structures. It was found that

NiO_2 has a positive free energy of formation which shows that this structure is not preferred. This matches experiment as the NiO_2 phase is not seen in the Ni Pourbaix diagram. However, the doping of Co, Fe, and P shows that this phase has a negative $\Delta G°_{f..}$

The change in Gibbs energy for the oxidation of Ni was calculated using the following equations:

$$\Delta G_{(Ni2+ \rightarrow Ni3+)} = \Delta G_{f(NiOOH)} - [\Delta_f G_{(Ni(OH)2} + \mu H] \quad (1)$$

$$\Delta G_{(Ni3+ \rightarrow Ni4+)} = \Delta G_{f(NiO2)} - [\Delta_f G_{(NiOOH} + \mu H] \quad (2)$$

where μH is -3.73eV, and $\Delta G_{f(NiOx)}$ is the formation energy of the various structures as listed in Supplementary Table 2. Using experimental formation energy values for $Ni(OH)_2$ and NiOOH the $\Delta G_{(Ni2+ \rightarrow Ni3+)}$ is -2.39 eV which is in agreement with the calculated $\Delta G_{(Ni2+ \rightarrow Ni3+)}$ of -2.24 eV[46].

To account for the thermodynamics of the electrochemical environment we have calculated the $\Delta G_{(Ni2+ \rightarrow Ni3+)}$ and $\Delta G_{(Ni3+ \rightarrow Ni4+)}$ as a function of pH. The slope of the line is given by $E_0 = \Delta G°_f (Ni^{3+}) - \Delta G°_f (Ni^{2+}) - 0.05916*pH$ for the Ni^{2+} to Ni^{3+} oxidation and $E_0 = \Delta G°_f (Ni^{4+}) - \Delta G°_f (Ni^{3+}) - 0.05916*pH$ for the Ni^{3+} to Ni^{4+} oxidation. The plot (Supplementary Fig. 25) shows that at pH=7 the anodic potential window for Ni^{3+} to exist is much larger (0.2V – 1.1V) for the doped NiCoFeP catalyst than for Ni alone (1.07V – 1.29 V). Notice that at the applied potentials of 1.4V and above the Ni^{4+} species should be stable.

The β-NiO_x was chosen as a model system to study the effect of intimate elemental doping. The experimental catalyst is mainly amorphous without a crystalline LDH phase and thus it is not possible to accurately model such a system using DFT. We have chosen a model system assuming the preservation of local chemistry to study the effect of doping with other elements. This model system strategy has been previously employed to study an amorphous FeCoW oxyhydroxide OER catalyst[16]. In this case, we have chosen to incorporate P into a Ni site to investigate how a local P binding intimately to other metals through an oxygen may affect the energetics. We note if our

experimental catalyst was a crystalline LDH, that a γ-phase NiO_x structure with PO_4^{3-} intercalating between the layers would be accurate.

To be thorough, we have performed additional calculations where the P is incorporated as a PO_4^{3-} molecule intercalated into the structure of the NiO_x catalysts (Supplementary Fig. 24). It was found that when PO_4^{3-} is intercalated, the $\Delta G_{oxidation}$ was higher than when the P replaces a Ni in the structure. Interestingly, the doping with different elements influenced the energies far less when intercalated in between layers than when substituted. For example, $\Delta G_{(Ni2+ \rightarrow Ni3+)}$ is lowered by 0.51 eV when the P-substituted NiO_xP is doped to $NiFeCoO_xP$, but the $\Delta G_{(Ni2+ \rightarrow Ni3+)}$ is only lowered by 0.11 eV when NiO_x-PO_4 is doped to $NiFeCoO_x$-PO_4. Furthermore, the $\Delta G_{(Ni3+ \rightarrow Ni4+)}$ is not lowered by any significant amount when phosphate is intercalated between the layers suggesting that the Ni^{4+} phase is less likely with phosphate between the layers than when P is substituted into a Ni site. We performed P K-edge of $FePO_4$ and NiCoFeP at Beijing Light Source 4B7A beamline to illustrate the structure (Supplementary Fig. 5). We confirmed that P incorporated into NiCoFeP as phosphate form. We also note that our ICP-AES elemental analysis showed no leaching of the constituents. If P was incorporated as a phosphate in between layers of the metal oxyhydroxide catalyst, then presumably it would be easy for this phosphate to leach into solution. Therefore, we believe that P is intimately incorporated into the amorphous catalyst as a phosphate and not in between layers and our computational model is a reasonable approximation of our system. Therefore, we believe our models are reasonable considering that the experimental spectroscopy data gives evidence for Ni^{4+} only upon doping with Fe and Co which is in agreement with our simulations.

To test possible doping positions, we have randomly changed the positions of Fe, Co, and P in the NiO_2 compound. It was found that the formation energies for all compounds were within 0.03 eV of each other. Furthermore, the lattice constants between all configurations were found to be almost identical. Therefore, we believe that the specific doping positions would not significantly influence the formation energies or structures. The structures, energies, and lattice constants are shown below in Supplementary Fig. 22 and Supplementary Table 4.

To account for the thermodynamics of the electrochemical environment we have calculated the $\Delta G(Ni^{2+} \rightarrow Ni^{3+})$ and $\Delta G(Ni^{3+} \rightarrow Ni^{4+})$ as a function of pH. The slope of the line is given by $E0 = \Delta G°f\,(Ni^{3+}) - \Delta G°f\,(Ni^{2+}) - 0.05916*pH$ for the Ni^{2+} to Ni^{3+} oxidation and $E0 = \Delta G°f\,(Ni^{4+}) - \Delta G°f\,(Ni^{3+}) - 0.05916*pH$ for the Ni^{3+} to Ni^{4+} oxidation. The plot (Supplementary Fig. 28) shows that at pH=7 the anodic potential window for Ni3+ to exist is much larger (0.2V – 1.1V) for the doped NiCoFeP catalyst than for Ni alone (1.07V – 1.29 V). Notice that at the applied potentials of 1.4V and above the Ni^{4+} species should be stable.

L-edge simulation with the OCEAN code

The formalism of the Bethe-Salpeter equation can be found in Ref (*30*). The input DFT+U calculations are performed using norm-conserving pseudopotentials. Very large energy cutoff of 160 Ryd is used for the plane-wave basis set of the Kohn-Sham wavefunctions. The key part of the electron-core-hole interactions is the screened Coulomb interaction, which is obtained within the random phase approximation. A large number of empty bands up to 50 eV above the Fermi level are included in the calculations. A 6x6x6 k-grid over the Brillouin zone is used to produce the sXASspectra, which is convoluted with a 0.5 eV Lorentzian line shape.

Theoretical sXAS spectra of Ni^{2+} with multiplet effects is shown below (Supplementary Fig. 3). This spectrum is produced with a crystal field splitting of 2.0 eV, i.e., the 10Dq parameter used in the CTM4XAS code, which is estimated from the DFT+U calculation for the layered $Ni(OH)_2$ structure.

Because the multiplet calculations cannot accurately reproduce the relative alignment of different oxidation states, we adopt a hybrid spectral simulation scheme, i.e., using multiplet calculations to recapture the missing satellite features and relying on the screened Coulomb interaction used in the Bethe-Salpeter Equation to produce the relative energy shift from Ni^{2+} to Ni^{4+}. More specifically, our comparison with experiments is carried out as follow:

(a) Obtain the Ni^{2+} spectrum from CTM4XAS (blue curve in Supplementary Fig.

3) and align it with the Ni^{2+} experimental spectrum (black). The magnitude of the spin-orbit coupling and the multiplet peaks are in excellent agreement with the experiment. The absolute energy alignment with experiment for Ni^{2+}, E_{CTM}, is thus determined.

(b) In CTM4XAS, the multiplet splitting can be turned off by setting the Slater integrals Fpd = Gpd = 0, which means there is no Coulomb interaction between the electrons on the 2p core level and those on the 3d shell. Switching off the multiplet effects yields a spectrum with no side satellite features (red). Using the same energy shift (E_{CTM}) as obtained in the last step which indicates that the multiplet effects tend to split the spectrum into two main peaks. The lower energy peak of this pair was the one we aligned to experiment above.

(c) We propose that the multiplet-free spectrum in (b) enables a fair comparison between the CTM4XAS and the OCEAN calculation, which cannot describe multiplets. We therefore align the Ni^{2+} BSE spectrum (orange) with the multiplet-free one (red), which yields an absolute energy alignment for the BSE spectral simulation, E_{BSE}.

(d) Using E_{BSE} and the relative energy shift from Ni^{2+} to Ni^{4+} as predicted by BSE, we can determine the absolute alignment of the Ni^{4+} BSE spectrum (green).

(e) The Ni^{4+} BSE spectrum now appears at a slightly higher energy, about ~ 1 eV than the experimentally determined L3 edge of Ni^{4+} (gray).

Materials and Methods

Chemicals

Iron (III) chloride ($FeCl_3$), nickel (II) chloride hexahydrate ($NiCl_2•6H_2O$), cobalt (II) chloride ($CoCl_2$), sodium dihydrogen phosphate ($NaH_2PO_4•2H_2O$), ethanol (≥99.5%), propylene oxide (≥99%), Nafion solution (5wt%) and N, N-Dimethylformamide were purchased from Sigma-Aldrich. All the chemicals were used without further purification.

Synthesis of gelled oxyhydroxides

Gelled NiCoFeP oxyhydroxides were synthesized using a modified aqueous sol-gel technique[19]. $NiCl_2•6H_2O$ (2.45 mmol), anhydrous $FeCl_3$ (0.27 mmol), and $CoCl_2$ (0.27 mmol) were first dissolved in ethanol (2 mL) in a vial. $NaH_2PO_4•2H_2O$ (0.27 mmol) was dissolved in another solution of deionized water (DI) (0.23 mL) mixed with ethanol (2 mL) in a separate vial. All solutions mentioned above were cooled in an ice bath for 2 h in order to prevent uncontrolled hydrolysis and condensation which may lead to the formation of precipitate rather than gel formation. The Ni, Fe, and Co precursors were then mixed with the supernatant of ethanol-water mixture containing $NaH_2PO_4•2H_2O$ to form a clear solution. To this solution, propylene oxide (≈1 mL) was then slowly added, forming a gel. The NiCoFeP wet-gel was aged for 24 hours to promote network formation, immersed in acetone, which was replaced periodically for 5 days before the gel was supercritically dried using CO_2.

Gelled NiCoP oxyhydroxides were synthesized following a process similar to that of NiCoFeP oxyhydroxides except with the addition of $FeCl_3$ as iron precursor. $NiCl_2•6H_2O$ (2.45 mmol) and $CoCl_2$ (0.27 mmol) were first dissolved in ethanol (2 mL) in a vial. The rest steps and parameters are the same.

Gelled NiP oxyhydroxides were synthesized following a process similar to that of NiCoFeP oxyhydroxides except with the addition of $FeCl_3$ and $CoCl_2$ as iron and cobalt precursors. $NiCl_2•6H_2O$ (2.7 mmol) were first dissolved in ethanol (2 mL) in a vial. The rest steps and parameters are the same.

All other gelled controls (NiCoFe, NiCo and Ni oxyhydroxides) with no phosphorus were synthesized following a process similar to those with phosphorus, except with the addition of $NaH_2PO_4 \cdot 2H_2O$ in the mixture of water and ethanol.

Characterization

Transmission electron microscopy (TEM), high resolution TEM images (HRTEM), high-angle annular dark-field scanning transmission electron microscopy (HAADF-STEM), and electron energy loss spectroscopy (EELS) elemental maps after OER were taken on a Hitachi 2700C transmission electron microscope operated at 200 kV. The samples were prepared by dropping catalyst powder dispersed in ethanol onto carbon-coated copper TEM grids (Ted Pella, Redding, CA) using micropipettes and were dried under ambient conditions. The cross-section scanning electron microscopy images of thin film samples were acquired using a Hitachi SU8230 scanning electron microscope operated at 1.0 kV. Powder X-ray diffraction (XRD) patterns were obtained with MiniFlex600 instrument. Data were collected in Bragg-Brettano mode using 0.02° divergence with a scan rate of 0.1° s^{-1}. The atomic composition of samples was determined using Inductively Coupled Plasma Optical Emission Spectrometer (ICP-AES). Mass specific surface areas of the catalysts were determined via nitrogen Brunauer, Emmett, and Teller (BET) area measurements. N_2 adsorption-desorption isotherms of the catalysts were measured at -196^{o}C using Quantachrome Autosorb-1 MP analyzer. Prior to the measurements, the samples were outgassed under vacuum for 10 h at 100°C. The total surface areas are deduced from the isotherm analysis in the relative pressure range from 0.05 to 0.20. The masses of the samples were measured with an ultramicro balance.

In-situ X-ray absorption

X-ray absorption measurements at the nickel, Co and iron L-edges were performed at the spherical grating monochromator (SGM) beamline 11ID-1 at the Canadian Light Source. The window of the sample cells was mounted at an angle of roughly 45° with respect to both the incident beam and the detectors. All measurements were made at

room temperature in the fluorescence mode using Amptek silicon drift detectors (SDDs) with 1024 emission channels (energy resolution ~120 eV). Four SDDs were employed simultaneously. The scanning energy ranges of Ni, Co and Fe L-edges were set between 840 and 900 eV, 760 and 820 eV, and 690 and 750 eV, respectively. For every edge, the scanning time was 30 s and repeated for ten times, and the fluorescence of every edge was collected at the same absorption edge. The partial fluorescence yield (PFY) was extracted from all SDDs by summation of the corresponding metal L emission lines.

Saturation effects in the PFY measurements were noted in the ex-situ measurement due to the relatively large intensity of the multiplet feature in comparison with the main peak. While some saturation effects may be present in the data, the interpretation of the in-situ results are not consistent with simple saturation. In particular, the appearance of the high energy resonance on the L2 peak, which appears upon application of the bias voltage, could not result from spectral distortions.

The probing depth of PFY was evaluated via the composition and the density, assuming that the valence of Ni, Co and Fe in hydroxides are 2+, 2+ and 3+ respectively. The densities of $Ni(OH)_2$, $Co(OH)_2$ and $Fe(OH)_3$ are set as 4.1 g cm^{-3}, 3.6 g cm^{-3}, and 3.9 g cm^{-3}. And the densities of our samples were calculated via the molar ratio of different unitary hydroxides. The estimated probing depth is around 300 nm. Even though the thickness of our sample is larger than the probing depth (Supplementary Fig. 6), the nanoporous structure makes thick film possible for *in situ* SXAS.

NiO (Ni^{2+}), $LiNiO_2$ (Ni^{3+}), and potassium nickel(IV) paraperiodate $K_2Ni(H_2IO_6)_2$ (Ni^{4+}) references were measured at Beijing Light Source using the 4B9B beamline (Supplementary Fig. 4). $K_2Ni(H_2IO_6)_2$ (potassium nickel(IV) paraperiodate) is known to be prone to reduction. The blue curve is a mixture of Ni^{2+} and Ni^{4+} since Ni^{4+} is unstable (Supplementary Fig. 4a). The second peak of Ni L3-edge at 857.5 eV and Ni L2-edge around 875.1 eV decreased after exposing to air,

indicating that these two peaks are the characteristic peak of Ni^{4+} (Supplementary Fig. 4b). To obtain the spectrum for Ni^{4+}, we subtracted Ni^{2+} spectrum from the spectrum of potassium nickel(IV) paraperiodate $K_2Ni(H_2IO_6)_2$ (Ni^{4+}) reference and obtained a single-peak shape that agrees well with the simulated Ni^{4+} spectra (Fig. 2c). The L-edge spectra were calibrated by using the total electron yield spectrum of NiO, which have absorption maxima at 853.2 eV[29]. Calibration spectra were run before in situ experiment to monitor beam stability and resolution. Considering $LiNiO_2$ reference is air sensitive, we stored and prepared $LiNiO_2$ in a glove box.

To better clarify the advantage of soft x-ray absorption, we performed Ni K-edge of NiP, NiCoP, NiCoFeP at 1.8 V vs. RHE, and compared with that of Ni L-edge (Supplementary Fig. 6). Even though hard XAS can reveal d-states (Supplementary Fig. 6a), more details of 3d electronic structures have been blurred due to the 1s lifetime broadening and the forbidden dipole 1s-3d excitation, whereas soft XAS probes directly the 3d-states at the valence band and provides information about the electronic structure around the excited atom, which is sensitive to the local structure and chemical environment of 3d metals (Supplementary Fig. 6b). Ni K-edge could not give the accurate ratio of different oxidation states.

Sample Cell for *in-situ* X-ray absorption

The bodies of the sample cells were fabricated on an Object Connex500 printer by 3D printing with DurusWhite material. The design of the electrochemical flow cell was adapted from a previously used flow cell[46]. Silicon nitride membrane windows (1 mm × 1mm × 100 nm) in Si frames (5 mm × 5mm × 525 μ m) were purchased from SPI Supplies. For electrochemical flow cells, the windows were treated by HF, and then coated by electron-beam evaporated titanium (10 nm) and gold (30 nm). The catalysts were coated on the windows via drop-casting with a thickness of 400 nm, which was shown in fig. S5 below prepared via the same procedure and parameters on FTO. The gold-covered window was contacted by gold wires. Silver and platinum wires were used as reference and counter electrodes. In the final step of assembly, the windows were glued to the cell body using Varian Torr seal epoxy, forming an electrolyte

chamber of ~1 mm height. The contact between the gold film on the windows of the electrochemical cell and the gold wire was monitored during the curing process of the epoxy.

Electrochemical Measurements

Electrochemical measurements were performed using a three-electrode system connected to an electrochemical workstation (Autolab PGSTAT302N) with built-in electrochemical impedance spectroscopy (EIS) analyzer. The working electrode were Au (111) single crystal electrodes purchased from MTI Corporation (U.S.). Ag/AgCl (with saturated KCl as the filling solution) and platinum foil were used as reference and counter electrodes, respectively.

To load the thin film of catalysts on Au (111), 4 mg of catalyst was dispersed in 4 ml N, N-Dimethylformamide. The thin layer was pin coated using the following parameters: spin speed = 5000 revolutions per minute (rpm), acceleration = 2500 rpm s^{-1} and spin time = 30 s.

To load the catalyst on a gold-plated Ni foam (thickness: 1.6 mm, Sigma), 20 mg of catalyst was dispersed in a mixture containing 2 ml of water and 2 ml ethanol, followed by the addition of 100 µL Nafion solution. The suspension was sonicated for 30 min to prepare a homogeneous ink. Gold-plated Ni foam with a fixed area of 0.5 x 0.5 cm^2 coated with water resistant silicone glue was drop-casted with 20 µL of the catalyst ink.

Cyclic voltammetry (CV) measurements at 50 mV s^{-1} were performed for 3 cycles prior to the record of linear scan voltammetry (LSV) at 1 mV s^{-1} for each sample. A diluted paste was prepared by dispersing 1 mg of catalyst powder in 1 ml N, N-Dimethylformamide, sonicating for 30 mins. Then, the working electrode was prepared by dripping 5 µl catalyst ink onto GCE.

The integrating reducing CO_2 into CO and oxidizing H_2O to O_2 were performed in a gas-tight two-compartment H-cell separated by a bipolar membrane (Fumasep FBM, purchased from Fuel Cell Store). CO_2 gas was delivered into the cathodic compartment at a rate of 5.00 sccm and was routed into gas chromatograph (GC, PerkinElmer Clarus 600). The GC was equipped with a Molecular Sieve 5A

capillary column and a packed Carboxen-1000 column. Argon (Linde, 99.999%) was used as the carrier gas. The GC columns led directly to a thermal conductivity detector (TCD) to quantify hydrogen and a flame ionization detector (FID) equipped with a methanizer to quantify carbon monoxide.

The number of active sites can be calculated via the following equation (3):

$$n_{Ni/Co} = \frac{Q_{Ni/Co} \times N_A}{F \times r_{Ni/Co}} \quad (3)$$

where Q_{Ni} is the integration area of Co redox peak from CV curves, N_A is Avogadro's constant, F is the Faraday constant, $r_{Ni/Co}$ is the molar ratio of Ni/Co, assuming that Ni^{2+}/Ni^{4+} is a two-electron process, Co^{2+}/Co^{3+} is a one-electron process. The TOF value was calculated from equation (4):

$$TOF = \frac{J * A * \eta}{4 * F * n} \quad (4)$$

J is obtained at overpotential = 350 mV, A is the geometric area, *F* is the Faraday constant and η is the Faradaic efficiency. *n* is the mole number of active atoms on the electrode, calculated from equation (3) above.

The parameters of NiCoFeP, NiCoP, and NiP are listed as Supplementary Table 5.

Arrhenius Apparent Activation Energy Determination

The sealed three-electrode glass cell was suspended in a thermostatic silicone oil bath. The electrodes were passed through holes in the lid with an O-ring slightly larger than the electrodes to minimize evaporative losses. Two holes for let-in and let-out tubes with CO_2 gas were also sealed with O-rings. The effect of temperature on the performance of the catalysts is clearly visible in Supplementary Fig. 13. As expected, the kinetics of the OER are increased at elevated temperatures, reflecting the temperature dependence of the chemical rate constant. The apparent electrochemical activation energy (E_a) for water oxidation can be determined using the Arrhenius relationship[46]

$$\left.\frac{\partial(\log\ i_k)}{\partial(1/T)}\right|_{\eta} = \frac{E_a}{2.3R} \quad (5)$$

where i_k is the kinetic current at η = 700 mV, T is the temperature, and R is the universal gas constant. The Arrhenius plots at η = 700 mV for NiCoFeP catalysts and controls are shown in Fig. 3c and Supplementary Fig. 14, which reveal a linear dependence on temperature. From the slope of the Arrhenius plot, the E_a can be extracted, listed in Table 1. NiCoFeP has a lowest activation energy of 27.00 kJ mol^{-1}.

Calibration of the reference electrode Ag/AgCl and Ag wire

The calibrations of Ag/AgCl reference electrode and Ag wire reference electrode were conducted in the standard three-electrode system (the same system as that for performance measurements) as reference electrodes, using Pt foil as working and counter electrodes. The 0.5M H_2SO_4 electrolyte (pH = 0.3) was pre-purged with Grade 4 H_2 overnight and continuously bubbled with H_2 with a flow rate of 25 ml min^{-1} during calibrations. LSV was run around +/- 100 mV between hydrogen evolution and oxidation, and the potential of zero current was recorded. The LSV curves were shown in Supplementary Fig. 16 below. The potential of zero current was around 0.2198V (including pH correction of 0.3*0.0591=0.0177V) for Ag/AgCl electrode and 0.3306V (including pH correction of 0.3*0.0591=0.0177V) for Ag wire electrode, i.e. $E_{Ag/AgCl(KCl, sat)}$ + 0.1108V = $E_{Ag\ wire}$, which is the same as the previous reported value[48]. Unless otherwise stated, all experiments were performed at ambient temperature (22 ± 2°C) and electrode potentials were converted to the RHE scale using E(RHE) = E(Ag/AgCl) + 0.202V + 0.059*pH and E(RHE) = E (Ag wire) + 0.313V + 0.059*pH

Supplementary Figures and Tables

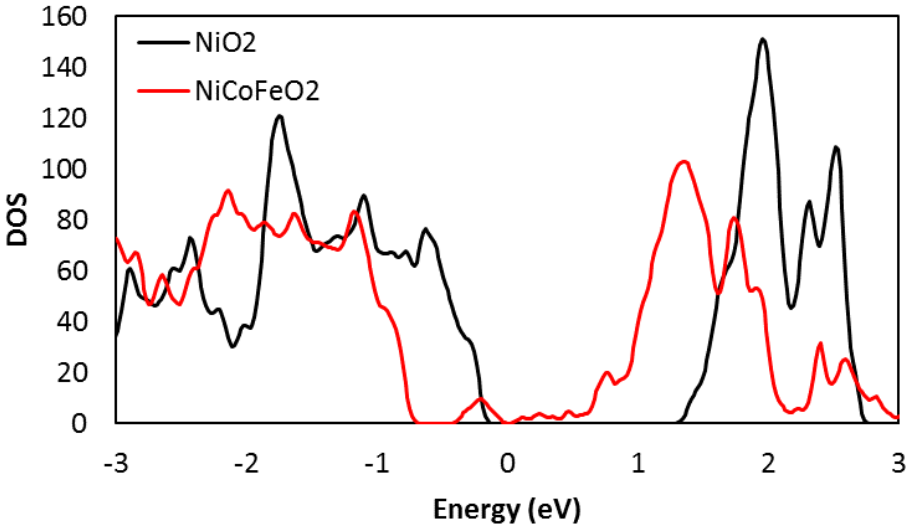

Supplementary Figure 1. DFT calculated total density of states for NiO_2 (black) and metal doped $NiCoFeO_2$ (red). Doping with Fe and Co introduces more electronic states between -0.5 eV and 1 eV, which may contribute to intermediate binding and increased catalytic activity.

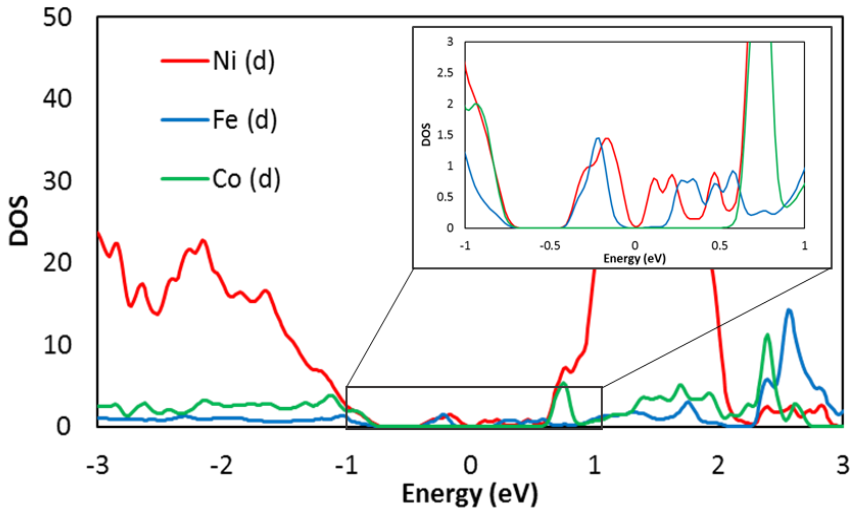

Supplementary Figure 2. Projected density of states of $NiCoFeO_2$ which has been extracted from the total DOS. The d-state contributions of Ni (red), Fe (blue), and Co (O) are shown. A zoom in graph between -1 eV and 1 eV show that Ni and Fe both have peaks in the pDOS whereas Co is essentially zero. This suggests that Ni and Fe can both contribute to catalytic activity whereas Co is inactive.

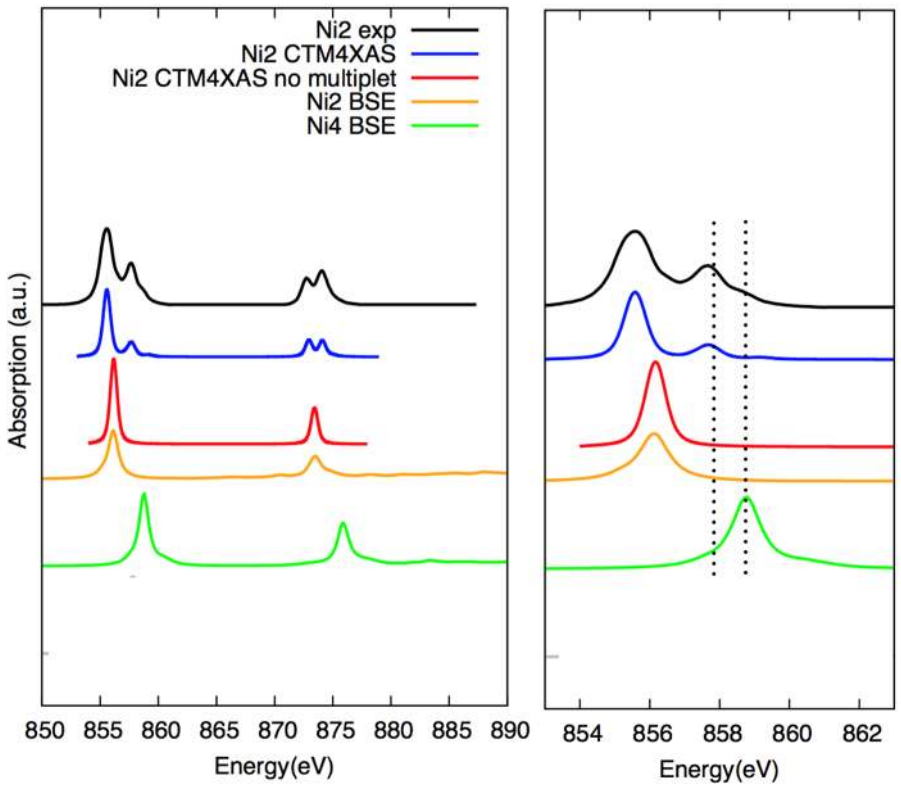

Supplementary Figure 3. Theoretical sXAS at the Ni L-edge of Ni^{2+} and Ni^{4+} by CTM4XAS and BSE calculations.

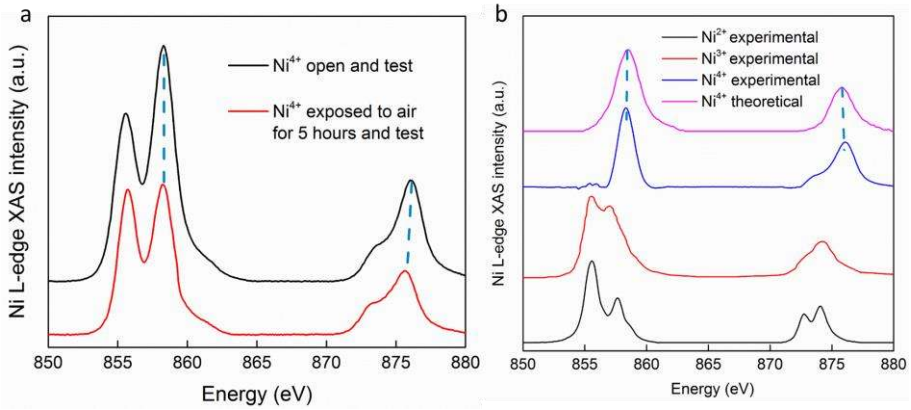

Supplementary Figure 4. (a) Ni L-edge of potassium nickel(IV) paraperiodat $K_2Ni(H_2IO_6)_2$ (Ni^{4+}) reference test immediately (black), and exposed to air for 5 hours (red). (b) Ni L-edge of NiO (Ni^{2+}), $LiNiO_2$ (Ni^{3+}), and potassium nickel(IV) paraperiodat $K_2Ni(H_2IO_6)_2$ (Ni^{4+}) references after subtracting Ni^{2+} signals.

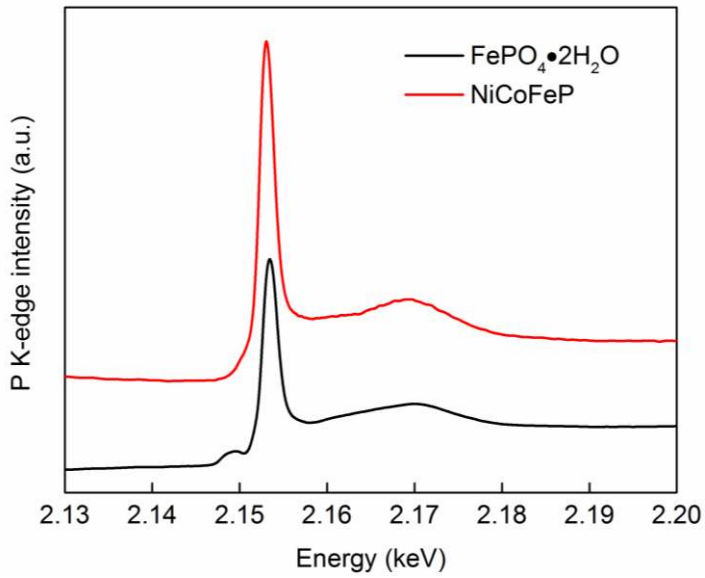

Supplementary Figure 5. P K-edge of $FePO_4$ reference and NiCoFeP catalysts.

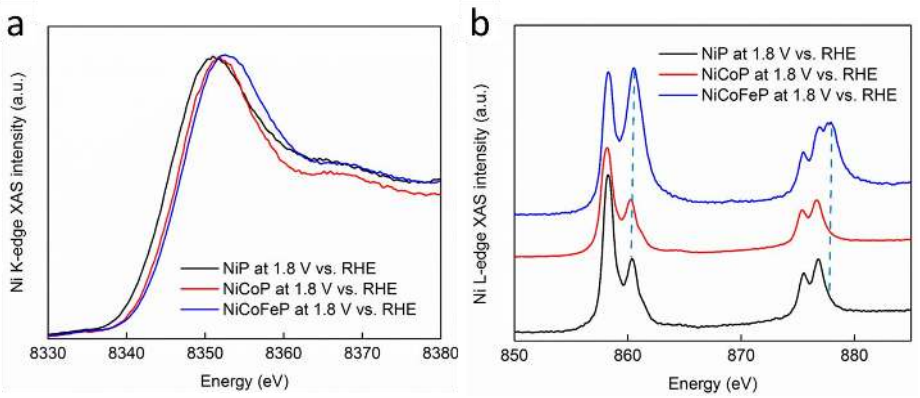

Supplementary Figure 6. Ni K-edge (a) and L-edge (b) x-ray absorption of NiP, NiCoP, and NiCoFeP at 1.8 V vs. RHE, respectively.

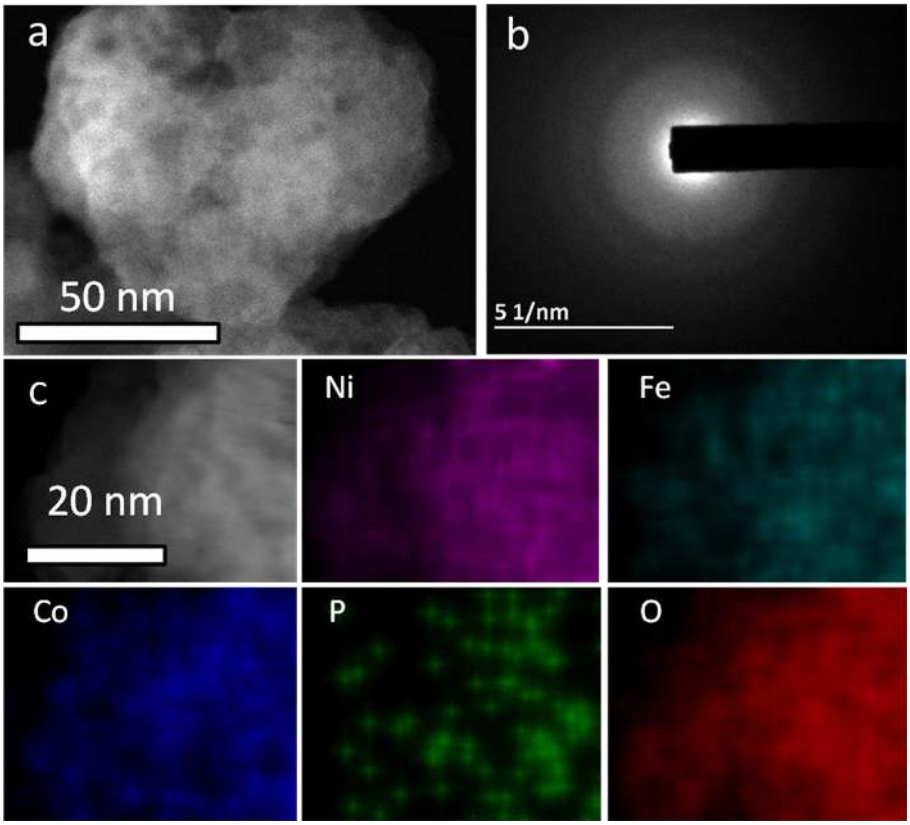

Supplementary Figure 7. Characterization of NiCoFeP oxyhydroxides catalysts. **a,** High-angle-annular-dark-field (HAADF) STEM image of nanoporous structure of NiCoFeP. **b**, Selected area electron diffraction (SAED) pattern. **c**, Energy-dispersive X-ray spectroscopy (EDS) elemental mapping from NiCoFeP oxyhydroxides sample.

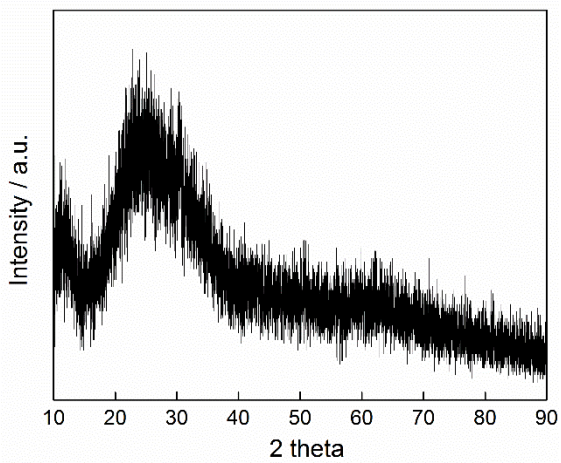

Supplementary Figure 8. X-ray diffraction (XRD) of NiCoFeP oxyhydroxide. NiCoFeP oxyhydroxide catalyst revealed no evidence for a crystalline phase.

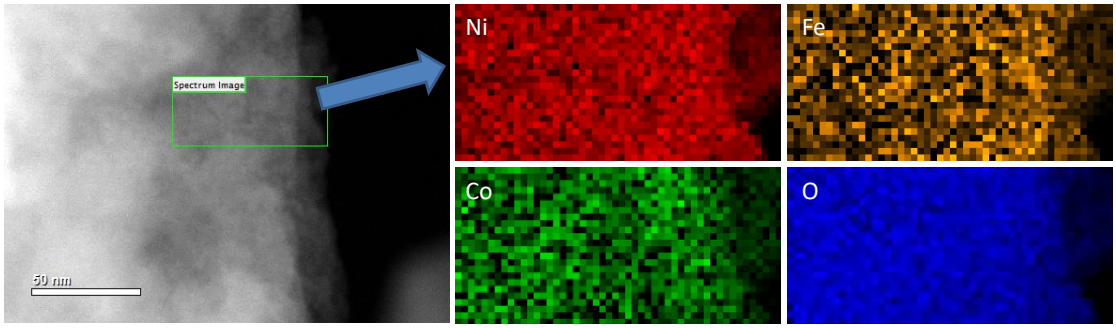

Supplementary Figure 9. Electron energy loss spectroscopy (EELS) elemental mapping from NiCoFeP oxyhydroxides catalysts.

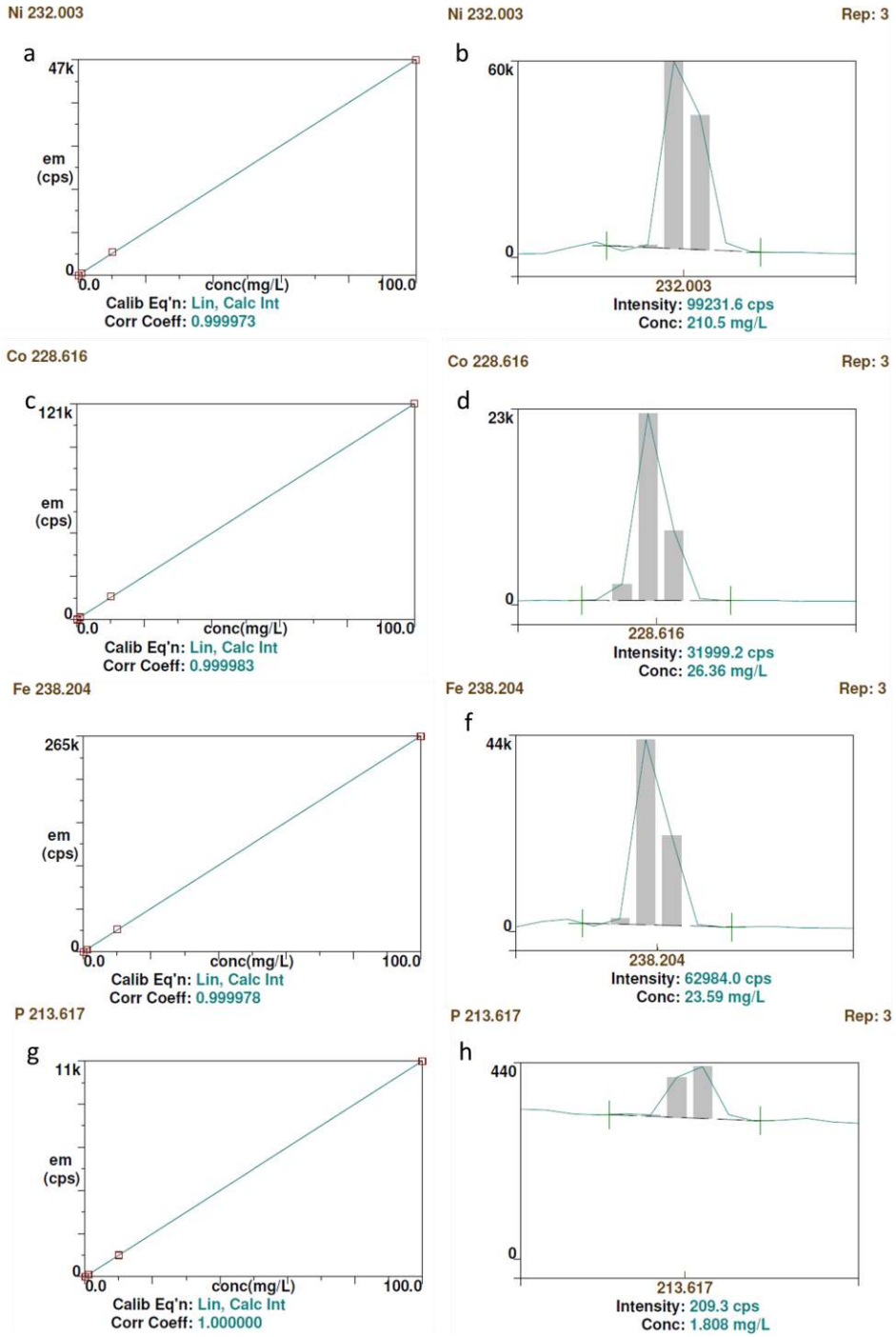

Supplementary Figure 10. Calibration curve of inductively coupled plasma atomic emission spectroscopy (ICP-AES) and ICP-AES spectra of NiCoFeP oxyhydroxides: Ni element (a, b), Co element (c, d), Fe element (e, f) and P element (g, h).

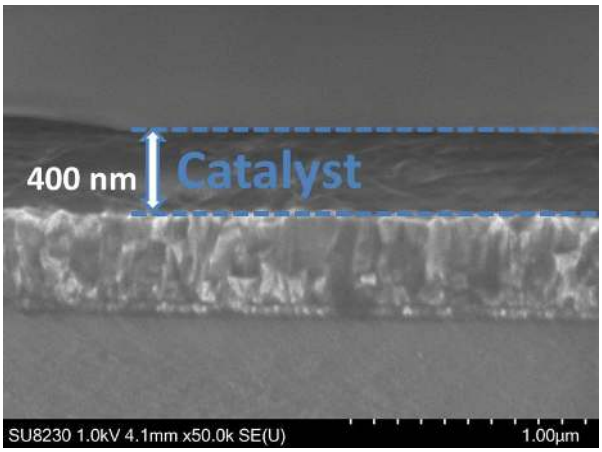

Supplementary Figure 11. Cross-section SEM image of NiCoFeP oxyhydroxides on FTO.

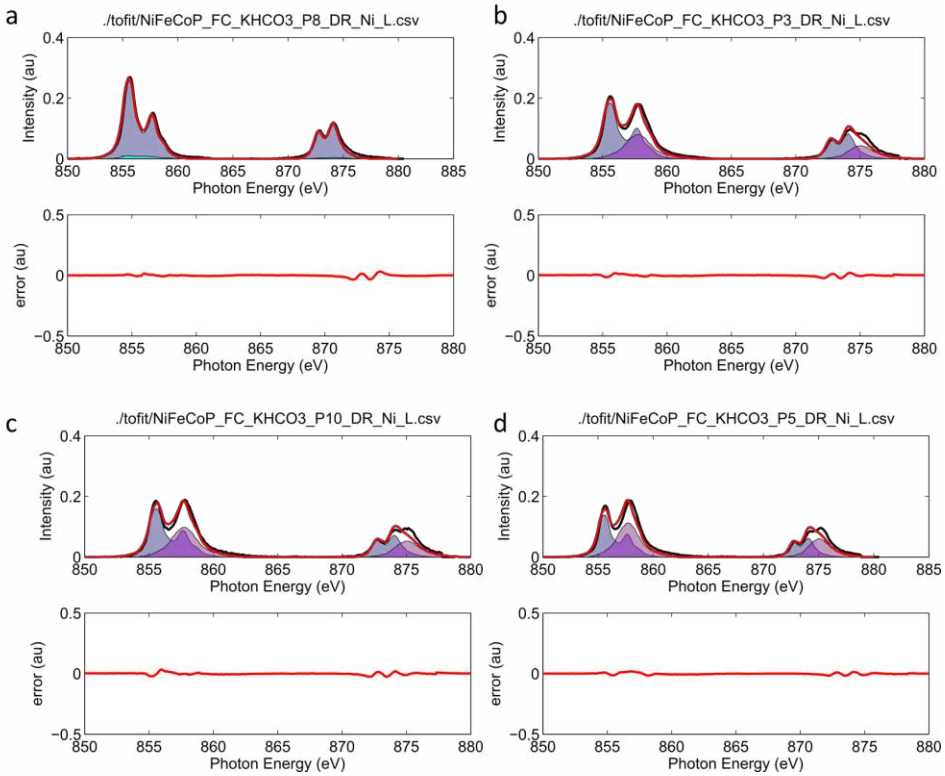

Supplementary Figure 12. Linear combination analysis of *in situ* Ni L-edge X-ray absorption spectra of NiCoFeP catalysts for Ni^{4+}, Ni^{3+}, and Ni^{2+} at 0V (a), 1.6V (b), at 1.8V (c) and at 2.0V (vs. RHE) (d). The black curves are the original data, the red curves are the fitting results, the blue filling areas are pure Ni^{2+} spectra, the cyan filling areas are pure Ni^{4+} spectra and the pink filling areas are pure Ni^{4+} spectra.

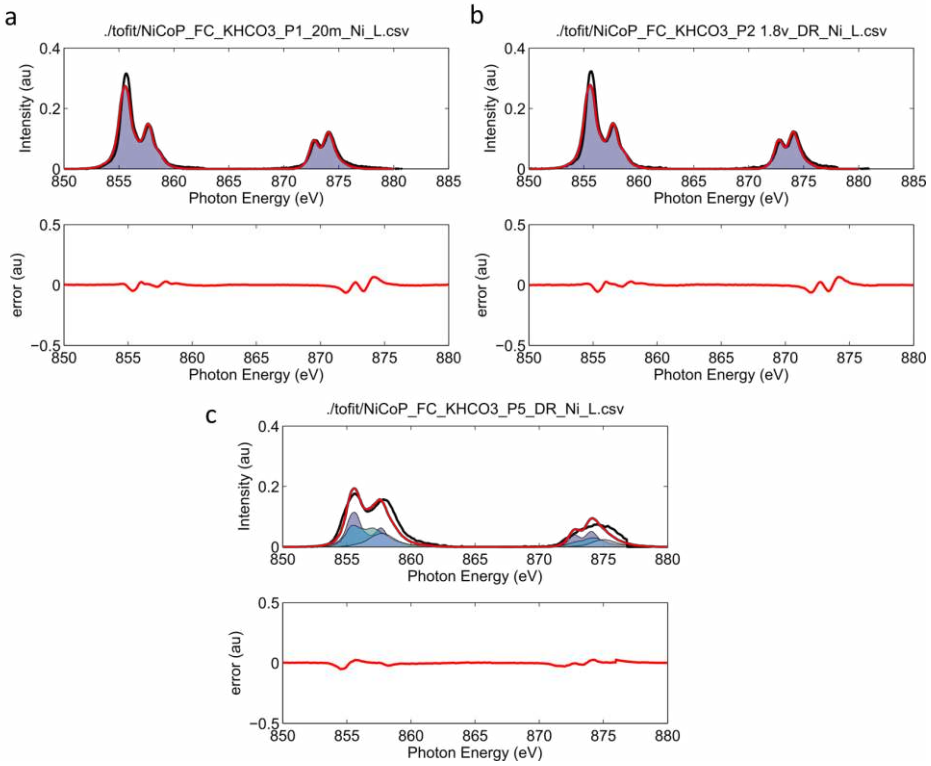

Supplementary Figure 13. Linear combination analysis of *in situ* Ni L-edge X-ray absorption spectra of NiCoP catalysts for Ni^{4+}, Ni^{3+}, and Ni^{2+} at 1.6V (a), at 1.8V (b) and at 2.0V (vs. RHE) (c). The black curves are the original data, the red curves are the fitting results, the blue filling areas are pure Ni^{2+} spectra, the cyan filling areas are pure Ni^{4+} spectra and the pink filling areas are pure Ni^{4+} spectra.

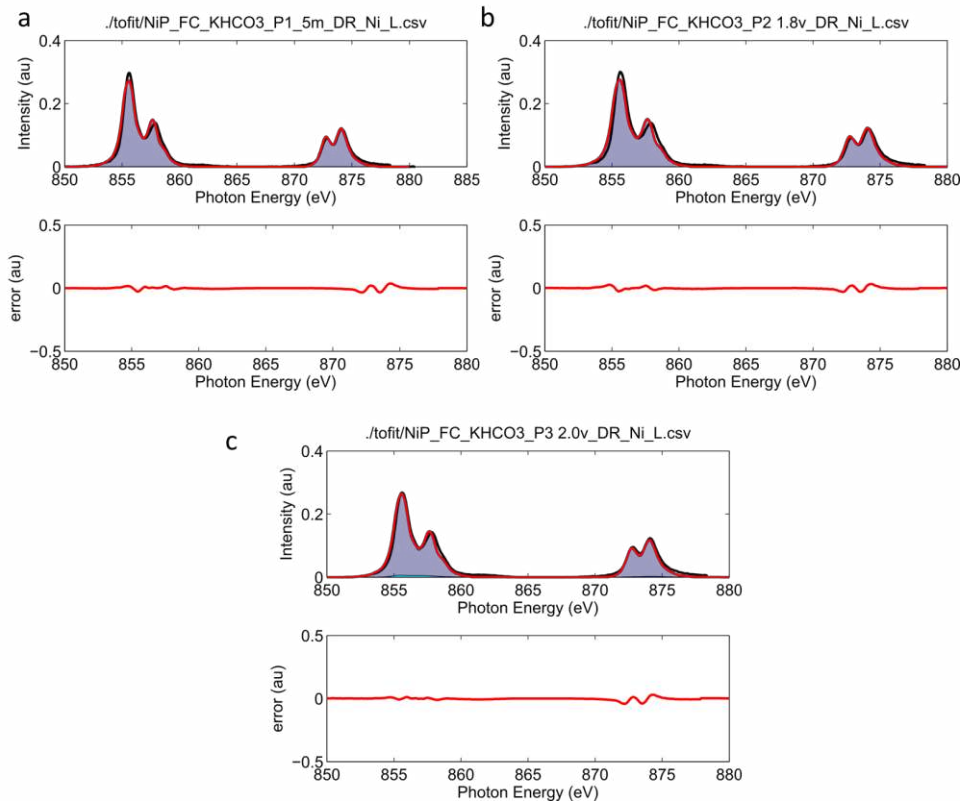

Supplementary Figure 14. Linear combination analysis of in-situ Ni L-edge X-ray absorption spectra of NiP catalysts for Ni^{4+}, Ni^{3+}, and Ni^{2+} at 1.6V (a), at 1.8V (b) and at 2.0V (vs. RHE) (c). The black curves are the original data, the red curves are the fitting results, the blue filling areas are pure Ni^{2+} spectra, the cyan filling areas are pure Ni^{4+} spectra and the pink filling areas are pure Ni^{4+} spectra.

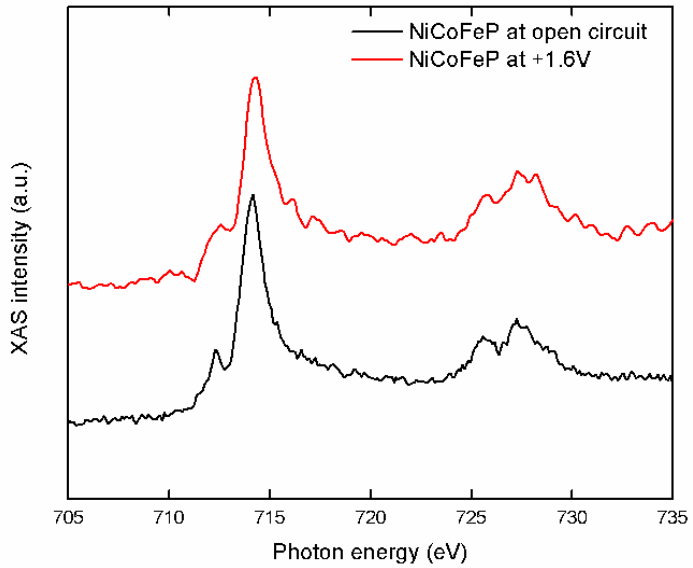

Supplementary Figure 15. Fe L-edge X-ray absorption spectra of NiCoFeP catalyst at open circuit and at +1.6V (vs. RHE).

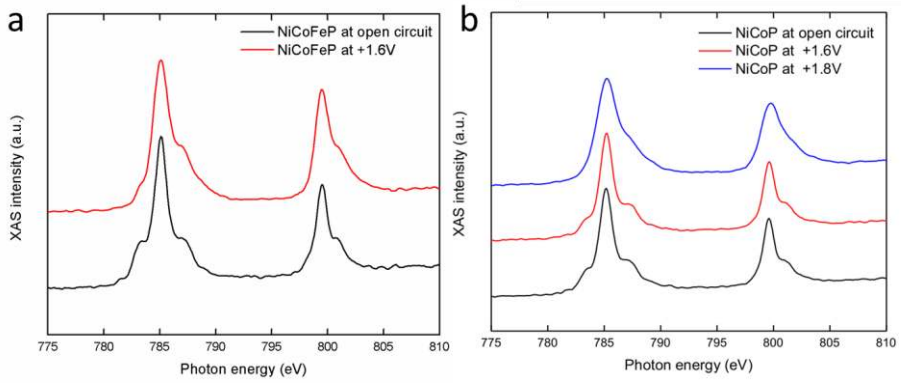

Supplementary Figure 16. Co L-edge X-ray absorption spectra of NiCoFeP (a) and NiCoP (b) catalysts at open circuit and at applied potentials (vs. RHE).

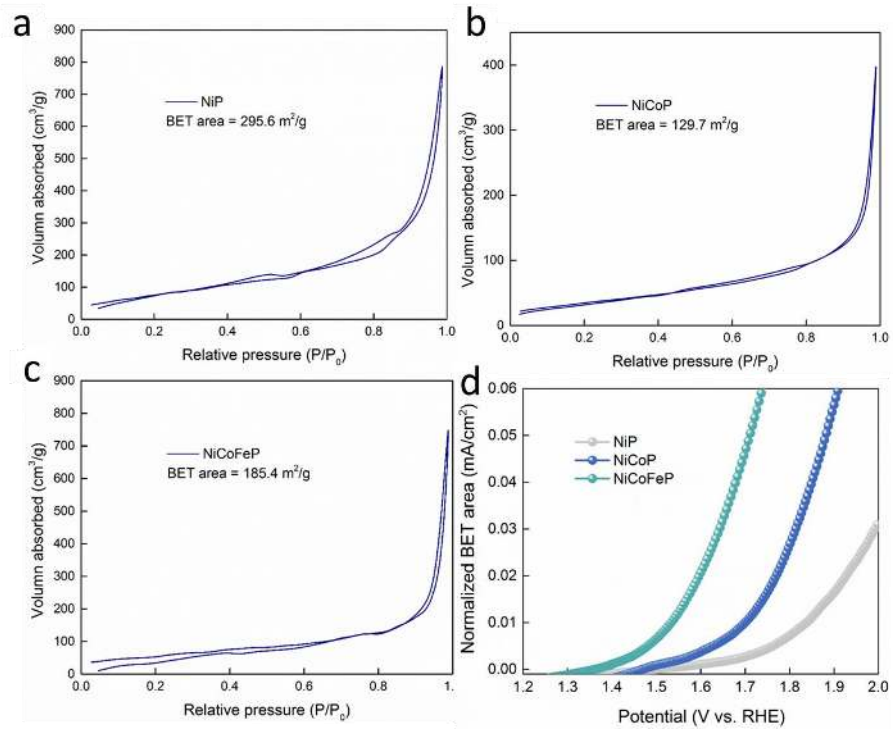

Supplementary Figure 17. N_2 sorption isotherms of (a) NiP, (b) NiCoP and (c) NiCoFeP oxyhydroxide; (d) LSV curves of NiCoFeP oxyhydroxides catalysts and controls in three configurations in CO_2 saturated 0.5 M $KHCO_3$ aqueous electrolyte loaded on Au foam and normalized by BET surface area.

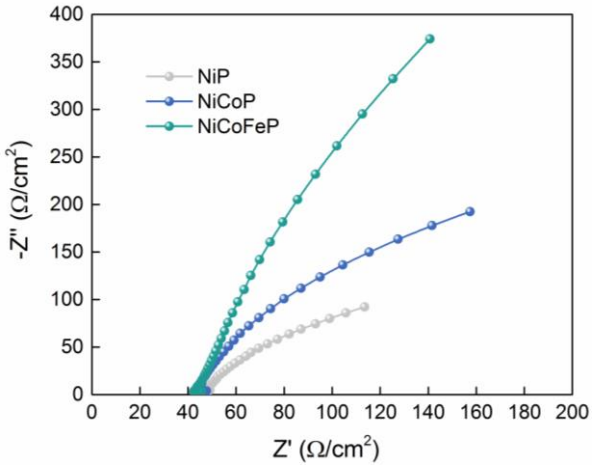

Supplementary Figure 18. Electrochemical impedance spectroscopy (EIS) data for NiCoFeP oxy/hydroxides catalysts and controls in three-electrode configuration in CO_2-saturated 0.5 M $KHCO_3$ aqueous electrolyte. The data were collected for the electrodes under 1.0 V vs. Ag/AgCl.

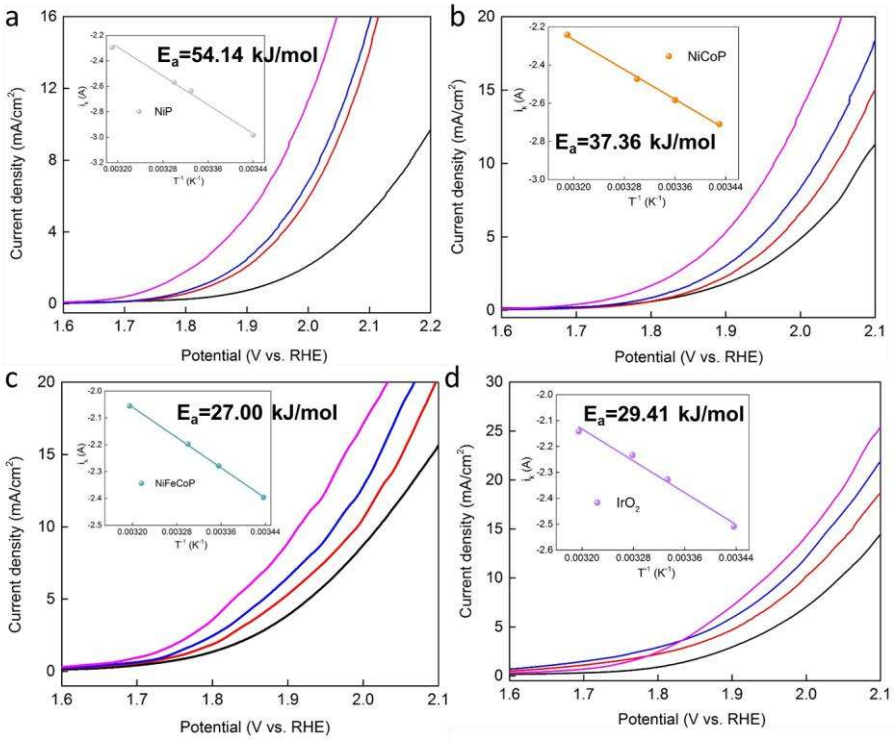

Supplementary Figure 19. The OER polarization curve of NiCoFeP oxyhydroxides catalysts and controls in three-electrode configuration in CO_2-saturated 0.5 M $KHCO_3$ aqueous electrolyte loaded on Au (111) with scan rate 1 mV s^{-1} at 18°C, 25°C, 30°C and 35°C, respectively. We considered the temperature effect when converting applied potential to relative hydrogen electrode potential.

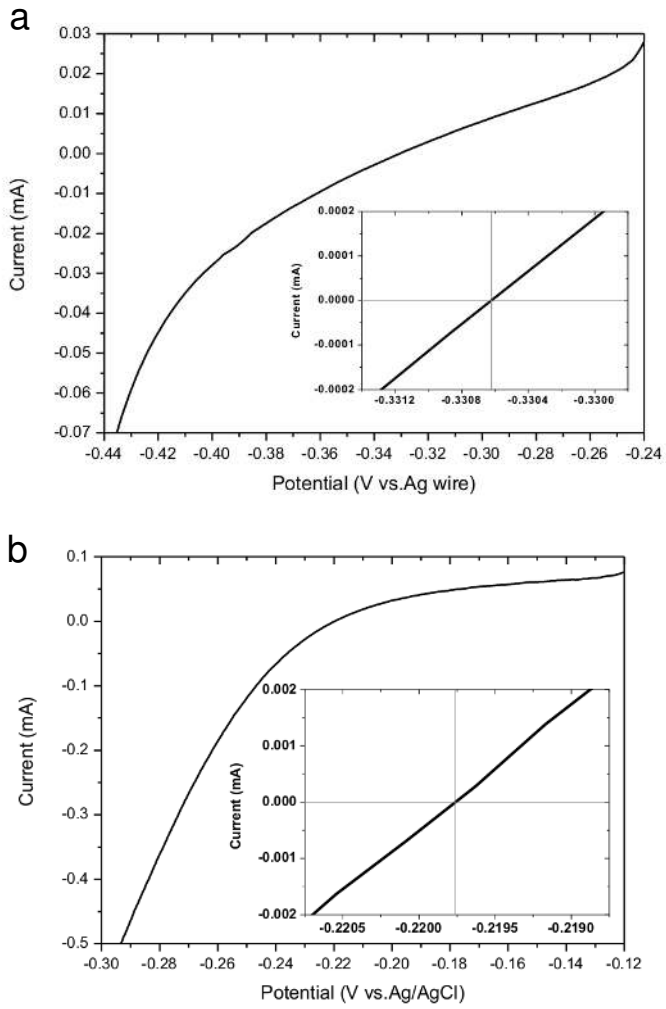

Supplementary Figure 20. Linear scanning voltammetric curves, sweeping the potential about +/-100 mV between hydrogen evolution reaction and hydrogen oxidation reaction, in three-electrode configuration in 0.5 M H_2SO_4 aqueous electrolyte bubbled with pure hydrogen gas, with scan rate 0.5 mV s^{-1}, at room temperature.

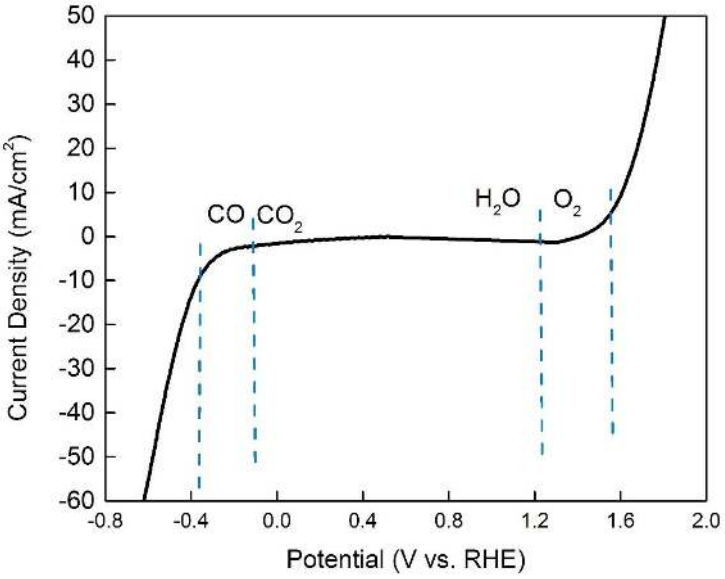

Supplementary Figure 21. Linear scanning voltammetric curves of NiCoFeP oxyhydroxides (right) and Au needles as CO_2 redcution catalysts (left). Theoretical oxidation and reduction potentials are $E^0_{O2/H2O}$= 1.23 V vs. RHE and $E^0_{CO2/CO}$= -0.11 V vs. RHE, respectively. Dashed lines represent the overpotential of OER and CO_2 reduction at 10 mA/cm^2.

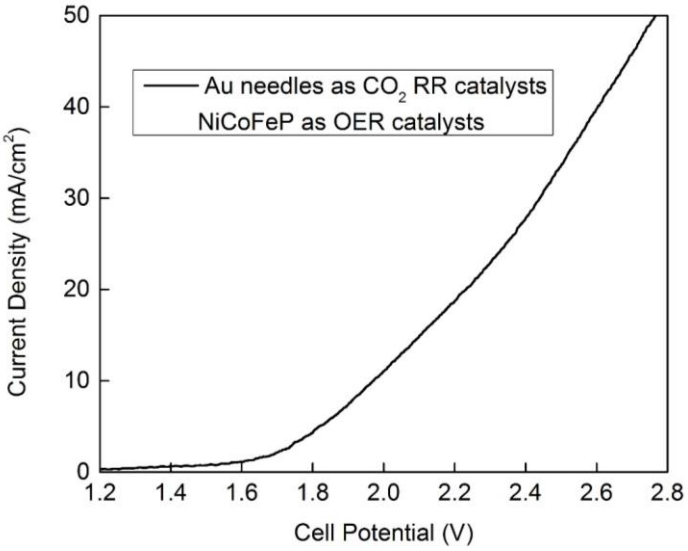

Supplementary Figure 22. Linear scanning voltammetric curves of NiCoFeP oxyhydroxides catalysts and Au needles in two-electrode configuration in CO_2-saturated 0.5 M $KHCO_3$ aqueous electrolyte with scan rate 5 mV s^{-1}.

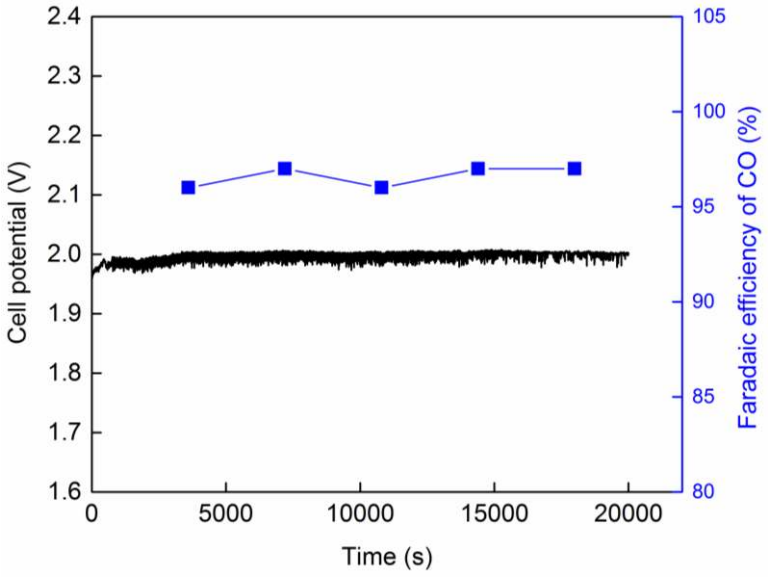

Supplementary Figure 23. Chronopotentiometric curves of NiCoFeP oxyhydroxides catalysts and Au needles in two-electrode system with constant current densities of 10 mA cm^{-2}, and the corresponding Faradaic efficiency from gas chromatography measurement of evolved CO.

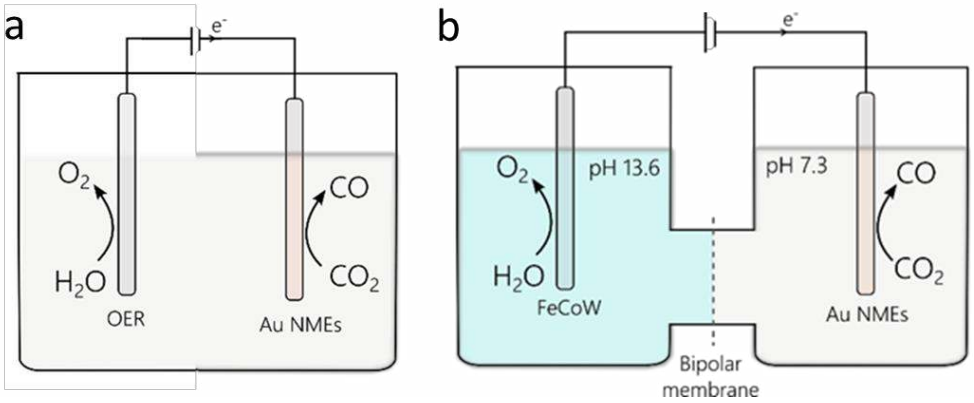

Supplementary Figure 24. (a) scheme of NiCoFeP-Au needles electrolysis; (b) scheme of FeCoW-Au needles electrolysis with bipolar membrane.

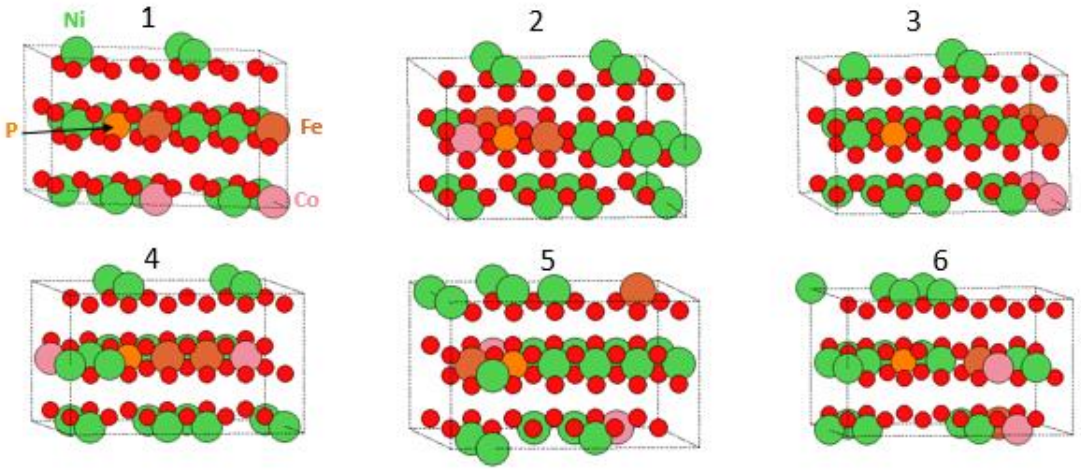

Supplementary Figure 25. Structures of $NiFeCoO_2P$ with differently doping positions. Ni (green), Fe (brown), Co (pink), P (orange), O (red).

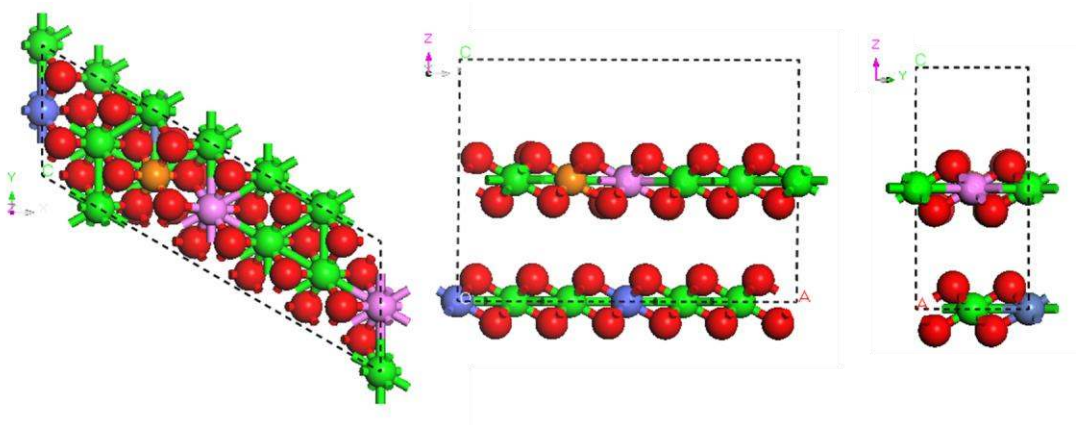

Supplementary Figure 26. Ball and stick representation of the optimal Ni^{4+} catalyst $NiFeCoO_2P$ with top view (left), front view (middle), and side view (right) where nickel is green, oxygen is red, cobalt is pink, iron is blue, and phosphorus is orange.

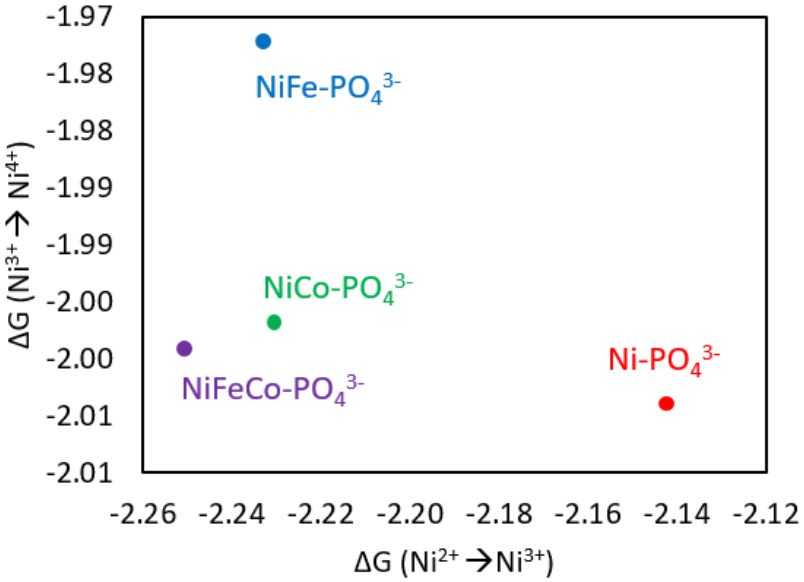

Supplementary Figure 27. ΔG of Ni^{2+} → Ni^{3+} and Ni^{3+} → Ni^{4+} where phosphate is intercalated between the layers of NiO_x (red), $NiFeO_x$ (blue), $NiCoO_x$ (green), $NiFeCoO_x$ (purple).

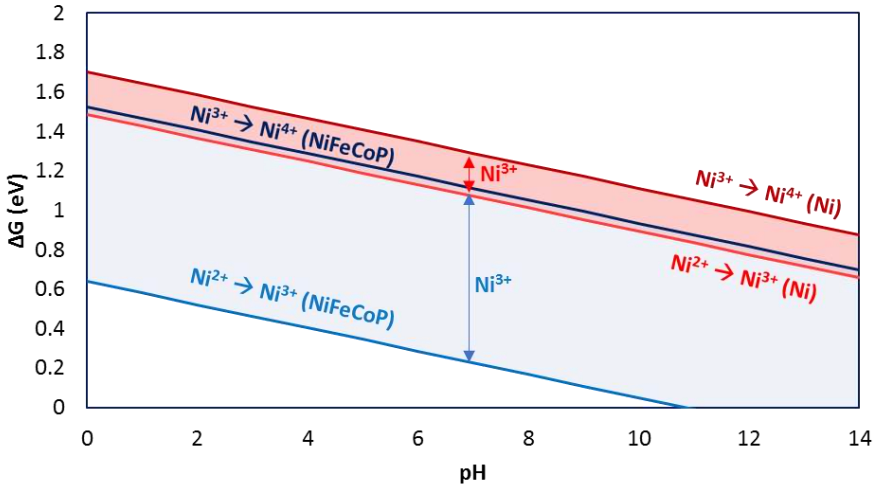

Supplementary Figure 28. A plot of calcualted $\Delta G_{(oxidation)}$ as a function of pH for pure Ni (red) and NiFeCoP(blue).

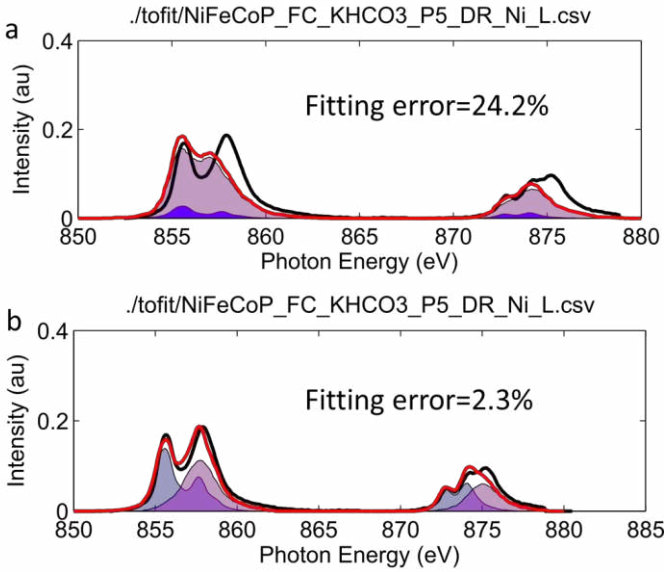

Supplementary Figure 29. Ni L-edge of NiCoFeP under an applied potential of 1.8 V vs. RHE fitted by (a) a combination of NiO (Ni^{2+}), $LiNiO_2$ (Ni^{3+}) references or (b) a combination of NiO (Ni^{2+}), $LiNiO_2$ (Ni^{3+}), and potassium nickel(IV) paraperiodate $K_2Ni(H_2IO_6)_2$ (Ni^{4+}) references, respectively. The black curves are the original data, the red curves are the fitting results, the blue filling areas are pure Ni^{2+} spectra, the cyan filling areas are pure Ni^{4+} spectra and the pink filling areas are pure Ni^{4+} spectra.

Supplementary Table 1. Lattice constants for all DFT optimized structures.

	a	b	c	α	β	γ
$Ni(OH)_2$	3.14	3.21	4.66	90.00	89.96	120.82
	(3.13)[a]	(3.13)[a]	(4.61)[a]	(90.00)[a]	(90.00)[a]	(120.00)[a]
β-NiOOH	2.97	2.89	4.95	82.66	93.25	119.96
	(2.93)[b]	(2.96)[b]	(4.84)[b]	(80.00)[b]	(90.00)[b]	(119.70)[b]
NiO_2	2.76	2.76	5.08	90.07	89.60	120.03
$Ni(OH)_2P$	3.17	3.24	4.71	89.72	90.14	121.53
β-NiOOHP	2.98	2.89	4.94	82.96	94.54	119.78
NiO_2P	2.76	2.76	5.10	90.15	89.60	120.03
$NiCo(OH)_2$	3.14	3.22	4.68	90.13	89.75	120.90
β-NiCoOOH	2.96	2.91	4.94	83.77	92.11	120.26
$NiCoO_2$	2.77	2.78	5.12	90.52	89.44	120.04
$NiCo(OH)_2P$	3.13	3.24	4.70	90.27	89.74	120.36
β-NiCoOOHP	2.96	2.91	4.90	83.41	92.00	119.97
$NiCoO_2P$	2.77	2.77	5.17	91.01	89.37	119.99
$NiCoFe\ (OH)_2$	3.16	3.23	4.68	90.15	89.79	120.91
β-NiCoFeOOH	2.98	2.93	4.96	83.98	91.85	120.42
$NiCoFeO_2$	2.78	2.79	5.09	90.09	59.59	120.12
$NiCoFe\ (OH)_2P$	3.14	3.24	4.69	90.31	89.94	120.15
β-NiCoFeOOHP	2.97	2.92	4.92	83.24	92.82	119.98
$NiCoFeO_2P$	2.79	2.78	5.17	90.43	89.36	120.08

Numbers listed in brackets are from literature. [a](Solid State Ionics 2010, 181, 1764− 1770), [b](J. Phys. Chem. C 2015, 119, 24315−24322).

Supplementary Table 2. DFT energies and Gibbs Formation energies for all structures.

	Energy (eV/fu)	ΔG°f
$Ni(OH)_2$	-24.89	-2.88
NiOOH	-19.68	-1.39
NiO_2	-14.25	0.31
$Ni(OH)_2P$	-24.86	-2.85
NiOOHP	-19.98	-1.70
NiO_2P	-14.56	-0.01
$NiCo(OH)_2$	-25.06	-2.93
NiCoOOH	-20.22	-1.82
$NiCoO_2$	-14.95	-0.28
$NiCo(OH)_2P$	-24.98	-2.86
NiCoOOHP	-20.50	-2.11
$NiCoO_2P$	-15.24	-0.57
NiCoFe $(OH)_2$	-25.33	-3.01
NiCoFeOOH	-20.52	-1.93
$NiCoFeO_2$	-15.21	-0.36
NiCoFe $(OH)_2P$	-25.22	-2.91
NiCoFeOOHP	-20.85	-2.27
$NiCoFeO_2P$	-15.59	-0.74

Supplementary Table 3. Comparison of CO_2 to CO system efficiency.

CO_2 to CO	Membrane	OER catalysts	CO_2 reduction catalysts	Overpotential at 10 mA/cm^2	efficiency	Reference
1	Membrane-free	NiCoFeP (neutral)	Au needles (neutral)[49]	1.99 V	64%	This work
2	Bipolar membrane	FeCoW (alkaline)[16]	Au needles (neutral)[49]	2.37 V	54%	This work
3	Nafion membrane	Co-Pi (neutral)[50]	Iron porphyrin (neutral)	2.5 V#	52%#	Ref (51)
4	Membrane-free	IrO_2 (neutral)	Au (neutral)	2.3 V	49%	Ref (3)
5	Nafion membrane	Perfluorinated cobalt (neutral)	Perfluorinated cobalt (neutral)	3.2 V	41.9%	Ref (52)
6	Nafion membrane	Ru complex (neutral)	Ru complex (neutral)	3.4 V#	39.4%#	Ref (53)

Cell potential at 1 mA/cm^2.

Supplementary Table 4. Formation energies and lattice constants for all $NiCoFeO_2P$ configurations.

Configuration	E_{form} (eV)	a	b	c	α	β	γ
1	-0.74	2.79	2.78	5.17	90.43	89.36	120.08
2	-0.75	2.78	2.78	5.12	90.35	89.66	120.05
3	-0.72	2.78	2.78	5.16	90.30	89.43	120.01
4	-0.74	2.78	2.79	5.11	90.16	89.66	120.16
5	-0.75	2.78	2.78	5.12	90.13	89.60	120.10
6	-0.74	2.78	2.78	5.13	90.20	89.68	119.93

Supplementary Table 5. Comparison of catalytic parameters of NiCoFeP, NiCoP, and NiP.

Samples	Overpotential (mV) at 10 mA/cm^2	Tafel slope (mV dec^{-1})	TOF calculated by intergration of Ni/Co redox	BET surface area (m^2/g)	ΔH (kJ mol^{-1}) at η=700 mV	Rs from EIS (Ω)
NiP	588	98	0.26	295.6	54.14	43
NiCoP	547	85	0.48	129.7	37.36	42
NiCoFeP	330	60	0.68	185.4	27.00	42

Structures of Models Used

Structural models and the VASP POSCAR files of all optimized structures used in this study are listed in a separate file.

References and notes

36 Kazimirov, V. Y. *et al.* Atomic structure and lattice dynamics of Ni and Mg hydroxides. *Solid State Ionics* 181, 1764-1770, (2010).

37 Kresse, G. & Joubert, D. From ultrasoft pseudopotentials to the projector augmented-wave method. *Phys. Rev. B* 59, 1758-1775 (1999).

38 Solcà, R. *et al.* Efficient implementation of quantum materials simulations on distributed CPU-GPU systems. *Phys. Rev. B* 54, 1-12, (2015).

39 Li, Y.-F. & Selloni, A. Mechanism and Activity of Water Oxidation on Selected Surfaces of Pure and Fe-Doped NiOx. *ACS Catal.* 4, 1148-1153, (2014).

40 Blöchl, P. E. Projector augmented-wave method. *Phys. Rev. B* 50, 17953-17979, (1994).

41 Miwa, K., Ohba, N., Towata, S.-i., Nakamori, Y. & Orimo, S.-i. First-principles study on lithium borohydrideLiBH4. *Phys. Rev. B* 69, (2004).

42 Cococcioni, M. & de Gironcoli, S. Linear response approach to the calculation of the effective interaction parameters in theLDA+Umethod. *Phys. Rev. B* 71, (2005).

43 Costanzo F. Effect of doping beta-NiOOH with Co on the catalytic oxidation of water: DFT+U calculations. Phys Chem Chem Phys 2016, 18(10): 7490-7501.

44 Monkhorst, H. J. & Pack, J. D. Special points for Brillouin-zone integrations. *Phys. Rev. B* 13, 5188-5192, (1976).

45 Balsara, N. P. & Newman, J. Comparing the Energy Content of Batteries, Fuels, and Materials. *J. Chem. Educ.* 90, 446-452, (2013).

46 Risch, M. *et al.* Reversibility of Ferri-/Ferrocyanide Redox during Operando Soft X-ray Spectroscopy. *J. Phys. Chem. C* 119, 18903-18910, (2015).

47 Anderson, A. B. *et al.* Activation energies for oxygen reduction on platinum alloys: Theory and experiment. *J. Phys. Chem. B* 109, 1198-1203 (2005).

48 Riskin, M., Basnar, B., Katz, E. & Willner, I. Cyclic control of the surface properties of a monolayer-functionalized electrode by the electrochemical generation of Hg nanoclusters. *Chemistry* 12, 8549-8557, (2006).

49 Liu, M. *et al*. Enhanced CO_2 Reduction Catalysts via Field-Induced Reagent Concentration. *Nature* accepted.

50 Liu, C. *et al*. Water splitting–biosynthetic system with CO_2 reduction efficiencies exceeding photosynthesis. *Science* 352, 1210-1213 (2016).

51 Tatin, A., Comminges, C., Kokoh, B., et al. Efficient electrolyzer for CO_2 splitting in neutral water using earth-abundant materials. *PNAS* 113, 5526-5529 (2016).

52 Morlanés, N., Takanabe, K. & Rodionov, V. Simultaneous Reduction of CO_2 and Splitting of H_2O by a Single Immobilized Cobalt Phthalocyanine Electrocatalyst. *ACS Catalysis* 6, 3092-3095, (2016).

53 Chen, Z. et al. Splitting CO_2 into CO and O_2 by a single catalyst. PNAS 109, 15606-15611, (2012).